A Low Resistance Calcium/Reduced Titania Passivated Contact for High Efficiency Crystalline Silicon Solar Cells

Thomas G. Allen, James Bullock, Quentin Jeangros, Christian Samundsett, Yimao Wan, Jie Cui, Aïcha Hessler-Wyser, Stefaan De Wolf, Ali Javey, and Andres Cuevas*

Recent advances in the efficiency of crystalline silicon (c-Si) solar cells have come through the implementation of passivated contacts that simultaneously reduce recombination and resistive losses within the contact structure. In this contribution, low resistivity passivated contacts are demonstrated based on reduced titania (TiO_x) contacted with the low work function metal, calcium (Ca). By using Ca as the overlying metal in the contact structure we are able to achieve a reduction in the contact resistivity of TiO_x passivated contacts of up to two orders of magnitude compared to previously reported data on Al/TiO_x contacts, allowing for the application of the Ca/TiO_x contact to n-type c-Si solar cells with partial rear contacts. Implementing this contact structure on the cell level results in a power conversion efficiency of 21.8% where the Ca/TiO_x contact comprises only ≈6% of the rear surface of the solar cell, an increase of 1.5% absolute compared to a similar device fabricated without the TiO_x interlayer.

1. Introduction

Advances in the efficiency of crystalline silicon (c-Si) photovoltaic (PV) devices above the long-held record efficiency value of 25% have all come from solar cell architectures with passivated contacts fabricated on n-type silicon.[1] The most successful devices to date have a silicon heterojunction (SHJ) cell structure, featuring a thin intrinsic amorphous silicon (a-Si) film that passivates c-Si surface defects, effectively separating the solar cell absorber (c-Si) from the remaining contact materials (doped a-Si, transparent conductive oxides, and metals). This separation of absorber and contact materials avoids extraneous Auger recombination and free carrier absorption losses associated with heavily doped regions, a detrimental feature of diffused junction solar cells. However, the amorphous silicon heterocontact structure necessitates the implementation of large contact fractions due to a relatively high contact resistivity. The trade-off between contact resistivity (ρ_c), contact recombination (J_{0c}), and contact fraction (f_c) is optimized for these devices by minimizing J_{0c} and combating the increase in ρ_c by applying the contacts over a large area. However, optical losses arising from parasitic absorption in the doped and intrinsic a-Si layers, as well as the transparent conductive oxide, are a limiting factor in this cell design.[2] Interdigitated back contact structures minimize these losses and have achieved the highest performance for c-Si solar cells,[3] but they still pose challenges for mass production.

Another strategy to achieve high efficiencies is to develop transparent, dopant-free, passivating heterocontacts that minimize ρ_c, thereby allowing the application of the contact structure to devices with low contact fractions, as in the partial rear contact (PRC) architectures commonly known as PERC (passivated emitter and rear cell) and PERL (passivated emitter with rear locally diffused) cells.[4] By minimizing ρ_c the constraints on recombination at the contact can be relaxed and the contact can be applied to small areas (f_c < 10%), leaving the remaining surfaces to be passivated with materials that have been utilized by the c-Si PV industry for decades, like silicon nitride (SiN_x) and aluminum oxide (Al_2O_3). These materials are known to effectively eliminate Shockley–Read–Hall, or defect-assisted, recombination at the silicon surface. Optically this approach

T. G. Allen, C. Samundsett, Dr. Y. Wan, Dr. J. Cui, Prof. A. Cuevas
Research School of Engineering
Australian National University
Canberra 0200, Australia
E-mail: thomas.allen@anu.edu.au
Dr. J. Bullock, Prof. A. Javey
Department of Electrical Engineering and Computer Sciences
University of California
Berkeley, CA 94720, USA
Dr. J. Bullock, Prof. A. Javey
Materials Sciences Division
Lawrence Berkeley National Laboratory
Berkeley, CA 94720, USA
Dr. Q. Jeangros
Department of Physics
University of Basel
Klingelbergstrasse 82, Basel CH-4056, Switzerland
Dr. Q. Jeangros, Dr. A. Hessler-Wyser
Institute of Micro Engineering
Photovoltaics and Thin-Film Electronic Laboratory
École Polytechnique Fédérale de Lausanne
Maladière 71b, CH-200 Neuchatel, Switzerland
Prof. S. De Wolf
KAUST Solar Center (KSC)
King Abdullah University of Science and Technology (KAUST)
Thuwal 23955-6900, Saudi Arabia

DOI: 10.1002/aenm.201602606

can be beneficial, insofar as these materials form nonabsorptive and highly reflective optical mirrors when common metals, like Al and Ag, are deposited on top of them. Nevertheless, very few dopant-free electron contacts have been found to date with a sufficiently low ρ_c to be applied to small contact fractions.

Recently, significant progress has been made in the development of directly metallized, dopant-free electron contacts applied to PRC cells fabricated on n-type silicon.[5,6] These device structures have been made possible by applying low work function materials to facilitate low resistivity ($\rho_c \approx 2$ mΩ cm^2) Ohmic contacts to undiffused n-type c-Si surfaces. These devices have demonstrated efficiencies of over 20%, but, like the PERC cell architecture, are limited by recombination at the contacts.[7,8] One promising material choice for the formation of a low resistance, dopant-free heterocontact is TiO_2, which has been recently demonstrated to form Ohmic contact on undiffused n-type silicon when applied in conjunction with a low work function Al/LiF overlayer, although no solar cells were fabricated due to the high contact resistivity ($\rho_c \approx$ 500 mΩ cm^2).[9] In addition, the work of Yang et al. has demonstrated full area Al/TiO_2 electron contacts on the rear side of 19.6% efficient n-type solar cells. With an additional SiO_x interlayer, these devices have shown a remarkable efficiency potential of up to 21.6%, however the application of these contacts is limited to large areas due to their relatively high contact resistivities ($300 > \rho_c > 30$ mΩ cm^2) even for TiO_2 thicknesses less than 3 nm.[10,11] In this article we show a reduction of up to two orders of magnitude in the contact resistivity of TiO_2 heterocontacts by replacing the overlying aluminum metal with the low work function metal calcium. In doing so, we demonstrate the compatibility of TiO_2 passivated heterocontacts with n-type c-Si cell designs with partial-area rear contacts, fabricating a first-of-its-kind passivated n-type PRC solar cell with an efficiency of 21.8%.

2. Results and Discussion

2.1. Surface Passivation

The passivation of c-Si surface defects by TiO_2 deposited by atomic layer deposition (ALD) has been demonstrated previously,[12–14] with surface recombination velocity (SRV; S_{eff}) values below 1 cm s^{-1} reported in the literature for TiO_2 films as thick as 15 nm on 10 Ω cm n-type silicon.[14] The work of Yang et al.[11] reports SRV values for thinner TiO_2 films in the range of 56–11 cm s^{-1} on 1 Ω cm n-type substrates for TiO_2 thicknesses between 2.5 and 5.5 nm, respectively (note that SRV scales with wafer doping in low injection conditions). All studies have reported deleterious effects of temperature on SRV, even for short annealing times at temperatures over 250 °C, a result of a phase transformation from amorphous to anatase TiO_2.[13,14]

The results of **Figure 1** display the effective minority carrier lifetime of silicon wafers coated with thin ALD TiO_2 layers after a thermal treatment in a forming gas ambient at 250 °C for 5 min, following the annealing optimizations in ref. [11] and [13]. The results show an increase in effective minority carrier lifetime with increasing TiO_2 thickness until saturating at

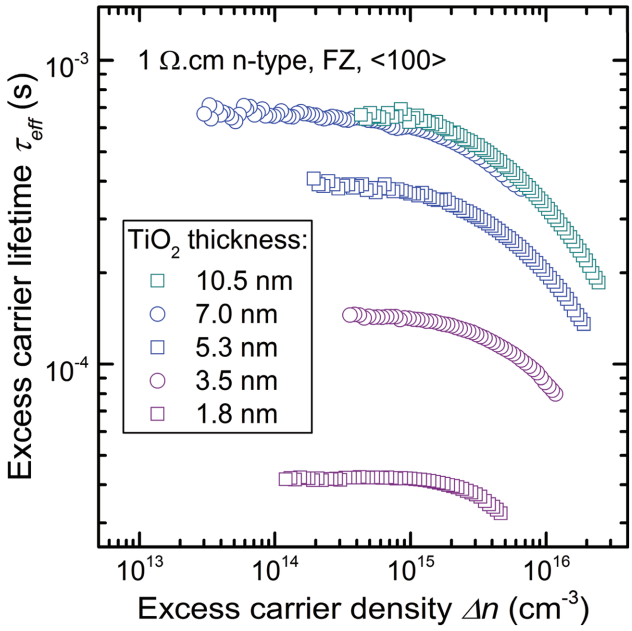

Figure 1. Excess carrier lifetime of TiO_2 passivated 1 Ω cm n-type silicon as a function of injection level measured using the photoconductance decay technique.

200 cycles. The SRV values, calculated using the intrinsic lifetime parameterization of Richter et al.,[15] are similar to those reported previously, ranging from ≈240 cm s^{-1} for the thinnest (1.8 nm) to 15 cm s^{-1} for the thickest TiO_2 layers (10.5 nm).

2.2. Contact Resistivity

Despite having been a common material for antireflection coatings in the c-Si PV industry, and despite its prevalent use in other solar cell devices (e.g., dye sensitized and perovskite solar cells), the capacity for TiO_2 to form an electron-selective heterocontact on c-Si has only recently been firmly established.[16] This finding prompted a number of studies into the efficacy of TiO_2 heterojunctions at the device level,[10,17] the most successful implementation of the Al/TiO_2 contact being that of Yang et al., which achieved a power conversion efficiency of 19.8%, increasing to 21.6% with the addition of a SiO_2 interlayer.[11] These devices feature full area TiO_2 contacts on the planarized rear of the solar cells as the contact resistivities of the Al/TiO_2 structures are not compatible with partial rear contact cell designs.

This limitation of the Al/TiO_2 contact is further demonstrated in **Figure 2**a, where the current densities extracted from Cox and Strack test structures are plotted as a function of voltage. The samples were fabricated on 0.9 Ω cm n-type Si wafers with a heavily phosphorus diffused, aluminum capped rear side to minimize the resistive contribution of the back contact. The undiffused front side feature TiO_2 layers of 3.5 and 5.3 nm contacted with Al; the *J*–*V* data from one control sample without TiO_2 is also shown in the figure. It can be seen that without the addition of the TiO_2 layer the direct n-type Al/Si contact exhibits a non-Ohmic, rectifying behavior typical

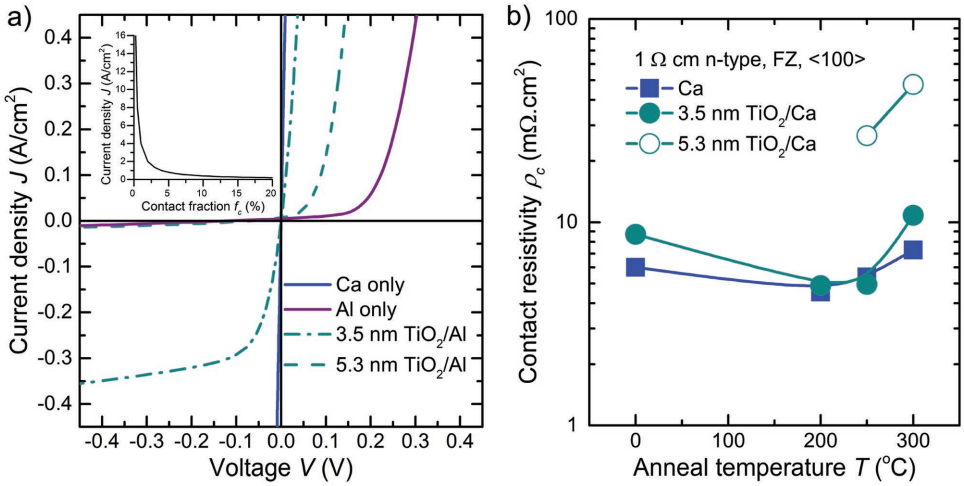

Figure 2. a) *J–V* measurements of contact resistance test structures showing rectifying (Schottky) behavior of the Al/n-type Si and Al/TiO_x/n-type Si contacts, and the Ohmic behavior of the Ca/n-type Si contact. b) Contact resistivity extracted from TLM test structures for Ca/Si and Ca/TiO_x/Si contacts.

of direct metal/undiffused n-type silicon Schottky contacts. The rectification observed is due to the formation of a large energy barrier for electrons (≈0.7 eV) at the Al/Si interface that is empirically ascribed to the Fermi-level pinning phenomenon, in which surface defects limit the metal work function's ability to influence the magnitude of the barrier height at the metal–silicon interface.[18,19] The addition of the 3.5 nm TiO_2 interlayer leads to a reduction of the barrier to electrons compared to the directly metallized case, however the *J–V* data is still representative of a non-Ohmic contact, contrary to the data in ref. [11]. If, however, we restrict the current density in Figure 2a to a range of ±0.1 A cm^{-2} the data appear Ohmic and an approximate extrapolation of $\rho_c \approx 150$ mΩ cm^2 can tentatively be made. Such is not the case for the thicker TiO_2 layer where the contact is rectifying at any reasonable current density range at the resolution of this measurement.

This interpretation of the *J–V* curves is relevant because the current density at the contacts in a solar cell is proportional to the inverse of the contact fraction (see the inset of Figure 2a). Very low contact fractions (e.g., $f_c = 1\%$) result in large current densities at an individual point contact, on the order of ≈4 A cm^{-2} for c-Si devices, while the current density at full area contacts mirrors that of the generation current (minus any quantum efficiency losses) and so is typically less than 0.04 A cm^{-2} at the maximum power point. This has a significant impact when interpreting contact resistance data and the applicability of contact structures to devices with large and small area contacts. This would also be a significant consideration when applying these contacts to concentrator cells which are more sensitive to resistive losses and where the generation current density approximately follows the concentration ratio. Additionally, for non-concentrator cells, the Al/TiO_2 contacts shown in Figure 2a applied to full areas would likely show a signature bending of the Suns-V_{oc} curve typical of rectifying contacts,[20] should a suitably high light intensity value be reached.[21] As such, the 3.5 nm Al/TiO_2 contact resistivity measured in Figure 2a is certainly suitable for non-concentrator cells with large area contacts, though the value of ρ_c is still higher than the value reported in ref. [11] but less than a prior report of 250 mΩ cm^2 for a similarly prepared contact structure.[10] The reason for this difference in reported ρ_c is unclear, however the assertion in refs. [10] and [11] of Ohmic contact for Al/TiO_2 test structures for TiO_2 thickness up to 5.5 nm may lie in a difference in the range of current densities explored.

The data of Figure 2a stand in contrast of that of Figure 2b, in which the low work function metal Ca is used as the contact material, instead of Al. As can be seen in Figure 2b, the addition of 3.5 nm of TiO_2 causes a negligible change in contact resistance over the directly Ca-metallized case ($\rho_c \approx 5$ mΩ cm^2), while increasing the thickness to 5.3 nm resulted in a non-Ohmic *I–V* response in the as-deposited state. After annealing at 250 °C, a ρ_c of 27 mΩ cm^2 was measured, increasing to 47 mΩ cm^2 with a further anneal at 300 °C, a trend of increasing ρ_c also registered for both the directly metallized and thinner TiO_2 samples. Using Al as the metallic overlayer, Yang et al. report contact resistivities of 250 and 750 mΩ cm^2 for TiO_2 layers of comparable thickness (3.5 and 5.5 nm, respectively),[10] indicating a remarkable reduction in contact resistivity of two orders of magnitude after replacing the Al layer with the low work function metal Ca.

While the ρ_c values measured for the thicker TiO_2 sample are not suitable for the application to devices with partial area contacts, and so are not further explored here, it may be that thicker TiO_2 layers result in lower J_{0c} values after metallization and so could be applied to larger contact areas. As the current focus is on passivated PRC cells we leave that optimization for future work.

2.3. PRC Solar Cells

The beneficial effect of the insertion of a TiO_2 passivating interlayer between the rear point contacts and the silicon absorber material in the PRC cell structure (depicted in the cell schematic of **Figure 3**a) is clearly demonstrated in the *J–V* curves of Figure 3b. Figure 3b compares the data from the cell reported

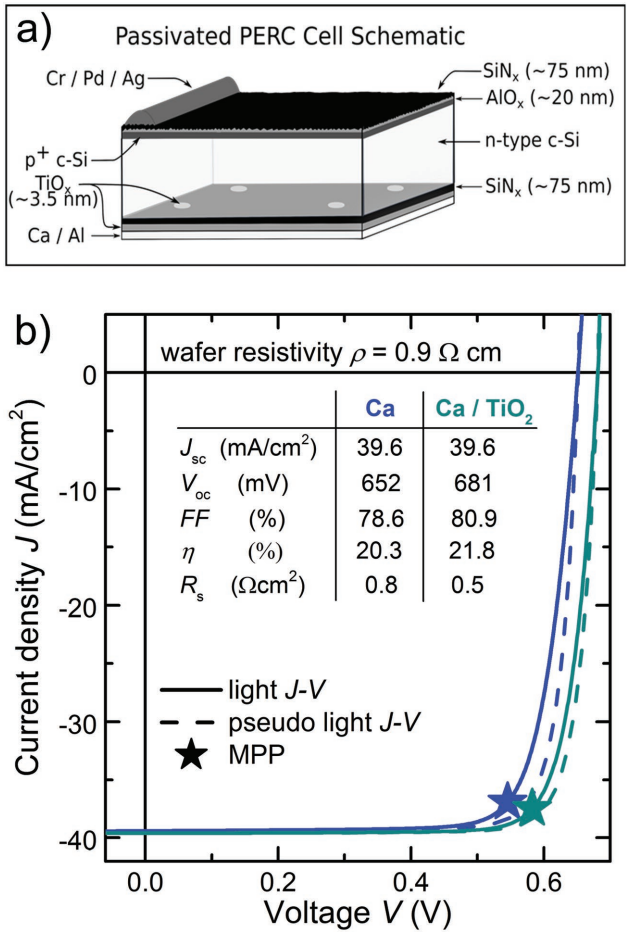

Figure 3. a) Schematic of the passivated, partial rear contact (commonly known as "PERC") solar cell structure fabricated in this study. b) One sun *J–V* curves of the PRC solar cells fabricated with and without a passivating TiO_x interlayer. Note that the TiO_x cell has a higher rear contact fraction (f_c = 6.25%) compared to the reference cell without the TiO_x (f_c = 1.26%).

in ref. [6] with a similarly fabricated device (this work) featuring both a larger rear contact fraction (6.25% vs 1.26%) and a 3.5 nm TiO_2 passivating interlayer between the Ca metal and the underlying c-Si absorber material. The TiO_2 passivating interlayer has increased the open circuit voltage of the device by nearly 30 mV to 681 mV, an increase in V_{oc} that is reflected in the increase in device efficiency by 1.5% absolute to 21.8%, making this device the most efficient c-Si solar cell with a TiO_2 heterocontact fabricated to date. Remarkably, this increase in efficiency is achieved without an increase in series resistance, but rather a decrease in R_s from 0.8 Ω cm^2 for the directly metallized cell to below 0.5 Ω cm^2. This is indicative of retention of the low contact resistance ($\rho_c \approx 5$ mΩ cm^2) despite the addition of the TiO_2 interlayer, as shown in the contact resistance data of Figure 2b, and also due to the application of the contact to a larger area. As the thin TiO_2 interlayer is transparent to IR wavelengths we measure no change in J_{sc}, while the increase in fill factor (FF) is a direct consequence of both the lower R_s losses and higher V_{oc}.

Despite the significant increase in V_{oc} measured on the passivated PRC cell, it is apparent from the superposition of the measured efficiency data on to the modeled curves of Figure S1 (Supporting Information) that the recombination rate at the Si/TiO_2 interface has increased markedly after the thermal evaporation of the overlying Ca layer. The minority carrier lifetime data of Figure 1 for a 3.5 nm thick TiO_2 passivating layer correspond to a J_{0c} of ≈5×10^{-14} A cm^{-2}. On the cell level the J_{0c} value increases to a value of $J_{0c} < 1 \times 10^{-11}$ A cm^{-2}, an increase of ≈2.5 orders of magnitude. Improving the J_{0c} value, either by a different choice of passivating interlayer, or through the insertion of a thin SiO_2 layer, as per ref. [11] remains critical to achieving device efficiencies competitive with other passivated contact technologies. Another pathway to higher efficiencies may lie in replacing the Ca layer with a less reactive, low work function material. Nevertheless, the device presented here represent the first n-type c-Si passivated partial rear contact cell and conclusively demonstrates the benefits of such a device architecture.

2.4. Structure and Composition of the Contact

The composition and stoichiometry of the as-deposited TiO_2 ALD layer has been analyzed by X-ray photoelectron spectroscopy (XPS). The survey scan (not shown) identified peaks in the spectra associated with Ti, and O elemental species as well as carbon contamination from the organic precursor. The Ti 2p core level spectrum, displayed in **Figure 4**, shows the peak positions of the Ti $2p_{1/2}$ (464.5 eV) and Ti $2p_{3/2}$ (458.7 eV) electron spin orbitals, a spin-orbit splitting of 5.8 eV, characteristic of Ti^{4+} species in TiO_2,[22–24] evidence of a stoichiometric as-deposited TiO_2 layer. The O1s spectrum (inset) has been deconvolved into two singlets: a main peak at 530 eV with a small shoulder at 531.6 eV. The main peak (O1s A) is representative of the direct oxygen (O^{2-}) bonding to the Ti^{4+} in stoichiometric

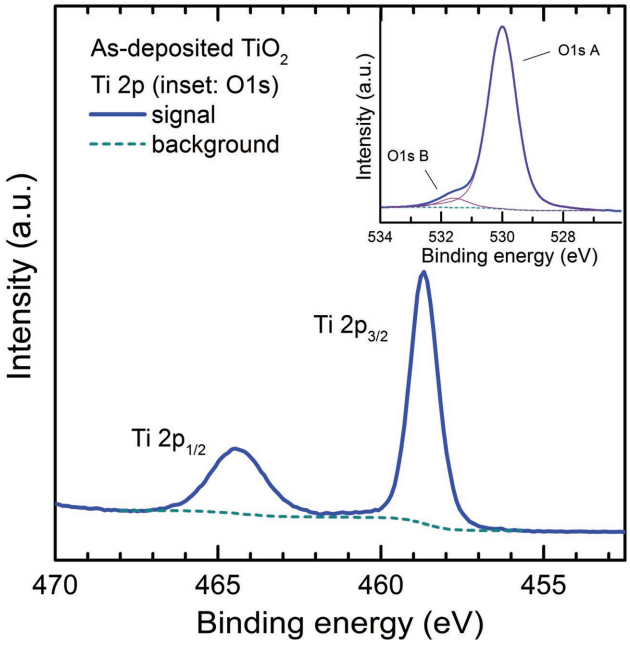

Figure 4. XPS of the ALD titania prior to metallization indicating a near stoichiometric atomic ratio of TiO_x, where $x \approx 2$ (inset: the O1s spectra).

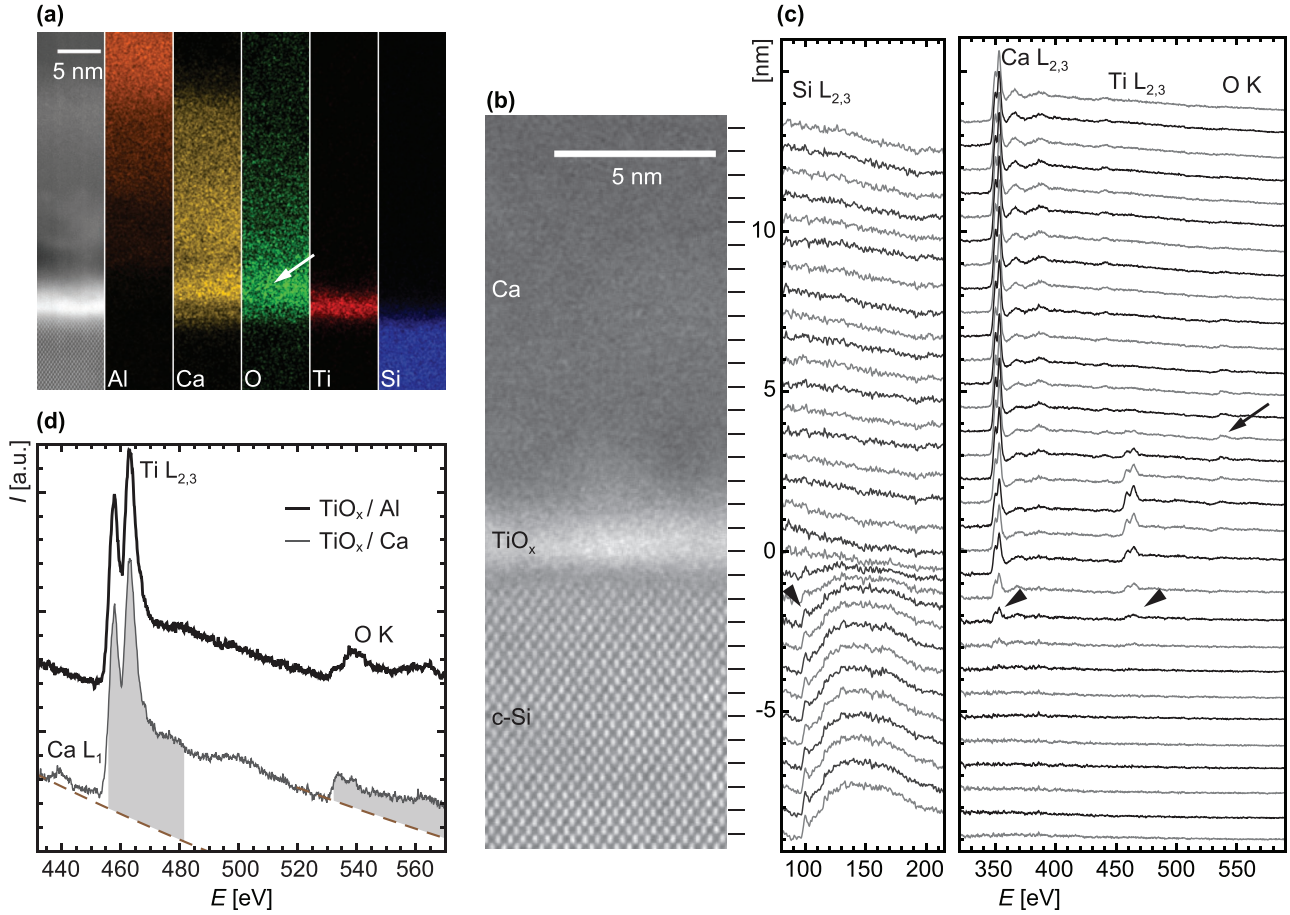

Figure 5. a) STEM HAADF imaging with EDX elemental mapping of the Al/Ca/TiO_x/Si contact structure. b) High resolution STEM with c) EELS of the same Al/Ca/TiO_x/Si contact. The EDX and EELS both show the Ca intermixing with the TiO_x layer. Higher energy resolution EELS taken from both the Al/TiO_x/Si and Ca/TiO_x/Si contacts are shown in d). Analysis of the high resolution EEL spectra indicates a reduction in the titania after the application of the contact metals.

TiO_2, while the shoulder (Os1 B) is often attributed to absorbed atmospheric oxygen (O_2) or hydroxyl (O—H) bonding from atmospheric H_2O, or perhaps residual H_2O from the deposition process.[25–28] Comparing the relative atomic percentages of the O and Ti components of the TiO_x layer indicates a near stoichiometric atomic ratio of $x \approx 2.09$. Excluding the oxygen content from the O1s B shoulder in the O1s spectrum reduces the atomic ratio to $x = 2$.

Scanning transmission electron microscopy (STEM) high-angle annular dark-field (HAADF) imaging coupled to energy-dispersive X-ray spectroscopy (EDX) or electron energy-loss spectroscopy (EELS) has been performed to further investigate the contact structure and composition after Al/Ca evaporation. The STEM HAADF micrograph and corresponding Al, Ca, O, Ti, and Si EDX maps shown in **Figure 5**a highlight the uniform titanium oxide layer separating the silicon absorber from the overlying Al/Ca contact metals. The EDX data also show an intermixing of the Al/Ca layers and the accumulation of O in the Ca layer close to the Ca/TiO_x interface. While the surface of the Ca is likely to have oxidized slightly during the transfer from the focused ion beam (FIB) to the transmission electron microscope (TEM), this effect should give rise to a more uniform O EDX signal at the position of the Ca layer than that observed in Figure 5a. Therefore, it is likely that the fluctuation in the O signal observed in the EDX image of Figure 5a arises from interactions between the TiO_x and the Ca layers.

Also observable in Figure 5a is the apparent diffusion of Ca through the TiO_x layer. This is supported by the EEL spectra (Figure 5c) recorded across the high-resolution STEM image shown in Figure 5b which detect Ca in the TiO_x layer. The EELS data also highlights some intermixing between Si, Ca, and Ti over ≈2 nm (arrowheads in Figure 5c), an observation that might be influenced by FIB-induced damage or the sample tilt. In agreement with the EDX, the EELS data demonstrate that O is present mainly on the Ca side of interface with the TiO_x layer (shown by the arrow in Figure 5c). Higher energy resolution EEL spectra of the Ti $L_{2,3}$ and O K edges of Ca/TiO_x and Al/TiO_x contact structures are shown in Figure 5d. In contrast to the stoichiometric TiO_2 composition inferred from the XPS data after deposition, an estimation of the Ti to O atomic ratio using EELS partial scattering cross sections yields a composition closer to TiO, irrespective of whether it is in contact with Ca or Al. The quantification procedure was performed using the software Digital Micrograph (Gatan, Pleasanton, USA) and involved the computation of a power law background (AE^{-r}, where E is the energy-loss in eV, A and r fitting parameters)

in the range 410–430 eV (for the Ti $L_{2,3}$ edges) and 513–528 eV (for the O K edge), the extrapolation of this background and its subtraction to the EELS signal in the range 456–476 eV and 532–572 eV, respectively, to yield the integrated Ti and O core loss intensities. These intensities are then related to elemental ratios using scattering cross sections (which have an accuracy on the order of 10%). It should be mentioned that while the shape of the Ti $L_{2,3}$ edges is indicative of its oxidation state, the amorphous nature of the TiO_x layer (as demonstrated in Figure 5b) complicates any fine structure fingerprinting procedure. Indeed, the lack of crystallinity prevents the splitting of the L_2 and L_3 edges into further peaks irrespective of the oxidation state, meaning that the fine structure of cubic (and presumably amorphous) TiO appears similar to that of amorphous TiO_2.[29,30] Overall, these results indicate that the Ca (and Al) uniformly reduces the neighboring TiO_2 layer to a stoichiometry closer to TiO_x, where $x \approx 1$. This, in part, can explain the build-up in oxygen at the Ca/TiO_x interface observed by EDX and EELS in Figure 5: evidence of the spontaneous migration of oxygen from the as-deposited stoichiometric TiO_2 to the overlying Ca layer.

The reaction kinetics of metal/TiO_2 interfaces have been studied by Fu and Wagner,[31] who found the interfacial reactivity (in this instance, the extent of O^{2-} transfer at the interface) to be dependent on the overlying metal work function. They demonstrated by XPS analysis on thin metal overlayers (≈6 Å) the reduction at room temperature of TiO_2 by Al, the lowest work function metal studied, which is in agreement with the EELS data shown in Figure 5d for the case of a direct contact between TiO_2 and Al. Since the work function of Ca ($\varphi \approx$ 2.9 eV) is considerably lower than that of Al ($\varphi \approx 4.2$ eV) it follows that the reduction of the TiO_2 would occur, and likely to a greater degree. Furthermore, the preceding interpretation of the EELS data suggesting the reduction of the TiO_2 to TiO is supported by the XPS data of Demri et al.,[32] in which the interface of crystalline TiO_2 and Ca was investigated. The authors also report on the formation on TiO and CaO layers due to the transfer of oxygen from the TiO_2 to the overlying thermally evaporated Ca layer. The reduction of TiO_2 by an overlying metal layer has also been proposed elsewhere as being critical to contact formation in TiO_x electron selective heterojunctions on c-Si, where the reduction in the titanium oxide is proposed to enhance electron transport through the layer by increasing its conductivity,[33] and either improving the band alignment with the silicon surface or reducing the barrier height at the metal/TiO_x interface.[11,34]

While there is a growing body evidence, including that presented here, suggesting a reduction in the TiO_x layer is one factor in enabling electron contact formation with c-Si, the presence of other effects complicates the analysis in this case. Of particular consideration is the difference in the work function of the contact metal used here, as opposed to other TiO_2/c-Si electron contacts reported in the literature. Given the similarities in EEL spectra in Figure 5d, it is apparent that the low work function of the Ca layer is one of the main drivers behind the reduction in ρ_c for the Ca/TiO_x, compared to the Al/TiO_x, contact. Additionally, the apparent reduction of the TiO_2 passivating layer implies an oxidation of the overlying, and interdiffused, Ca layer (and Al and Ti layers in ref. [11] and [34]). This may explain the sensitivity of ρ_c to TiO_2 thickness, though some presence of CaO_x is evidently tolerable in forming low contact resistivities. It is likely that both the change in stoichiometry of the TiO_x layer and possibly the diffusion of Ca into the TiO_x have had an impact on the passivation of the contact structure, explaining the large discrepancy in S_{eff} prior to metallization and the implied J_0 at the contact from Figure S1b (see Supporting Information). However, the extent to which each of the factors identified above are influencing the J_{0c} and ρ_c (and hence the device performance) is difficult to distinguish from the data.

3. Conclusion

The use of the low work function metal calcium has enabled the fabrication of a low resistance, dopant-free TiO_x passivated electron heterocontact to undiffused n-type c-Si substrates. The contact resistivity of the Ca/TiO_x/c-Si contact (≈5 mΩ cm^2) represents a reduction in ρ_c by two orders of magnitude over previously reported data for TiO_x/c-Si heterocontacts. Analytical transmission electron microscopy of the contact has revealed a reduction of TiO_2 layer by the overlying Ca metal that is likely to have assisted in the lowering of the contact resistivity but compromised the passivation of c-Si surface defects at the TiO_x/Si interface. Nevertheless, the extreme reduction in contact resistance compared to other TiO_x-based heterocontacts reported in the literature, as well as the reduction in recombination at the TiO_x/Si interface, has enabled the fabrication of a first-of-its-kind passivated partial rear contact n-type silicon solar cell with an efficiency of 21.8%, making this device the most efficient c-Si solar cell with a TiO_x heterocontact fabricated to date.

4. Experimental Section

The TiO_2 layers in this study were deposited by ALD (Beneq TFS 200) by sequential exposure of titanium isopropoxide (TTIP) and de-ionized water. The TTIP was heated to a temperature of 40 °C, while the deposition chamber was held at 230 °C. Symmetrically passivated lifetime samples were prepared on planar saw-damage etched, Radio Corporation of America (RCA) cleaned, silicon substrates that were dipped in dilute hydrofluoric acid (HF) prior to further processing. The effective lifetime (τ_{eff}) of the passivated samples was measured as a function of minority carrier injection level (Δn) on a Sinton Instruments WCT120 photoconductance tester operating in quasi-steady-state and transient modes. XPS (Thermo Scientific ESCALAB 250Xi) survey and core level scans were performed on the TiO_2 layers with a monochromatic Al Kα (1486.68 eV) X-ray source at a vacuum pressure of $<2 \times 10^{-9}$ mbar. The stoichiometry of the as-deposited TiO_2 was determined from the atomic percentage calculations taken from the XPS data after subtraction of the Shirley background using the software Advantage (Thermo Scientific, USA).

Thin, ≈30 nm, layers of Ca were thermally evaporated vacuum pressures $<1 \times 10^{-6}$ Torr from a solid source in a glovebox-integrated metal evaporator. An initial ≈150 nm capping layer of Al was sequentially evaporated in the same chamber without breaking vacuum. A further ≈150 nm of Al was subsequently evaporated after breaking vacuum to thicken the capping layer. Contact resistance measurements were performed using Cox and Strack (with a rear side Al/n^+ contact) and transfer length method (TLM) test structures which were fabricated using shadow masks to define the contact geometry.[35,36] The contact

resistivity was extracted from the *I–V* data obtained from a Keithley 2420 source meter.

The Al/Ca/TiO_2 and Al/TiO_2 contact structures were investigated on polished Si wafers by TEM. For this purpose, TEM samples were prepared using the FIB lift-out method in a Zeiss NVision 40 workstation and thinned down from the Si substrate side (to curtail possible redeposition of species) up to a final thickness of ≈80 nm using a final Ga^+ voltage of 2 kV to minimize surface damage and Ga implantation. To reduce Ca oxidation, the samples were quickly transferred from the FIB to a monochromated probe- and image-Cs-corrected FEI Titan Themis microscope, which was operated at 200 kV (air exposure of ≈2 min). Characterization then involved STEM HAADF imaging coupled to either EDX or EELS using a probe current of 250 or 50 pA, respectively. EEL spectra were recorded in Dual EELS mode using a Gatan GIF Quantum ERS high-energy resolution spectrometer and energy filter with a convergence semi-angle of 20 mrad and a collection semi-angle of 49 mrad. EEL spectra were acquired with an energy resolution of either 400 or 1200 meV depending on whether the monochromator was excited or not.

PRC solar cells (155 µm thick; 2 × 2 cm^2, isolated by a front-side mesa etch) were fabricated on 0.9 Ω cm n-type float zone (FZ) silicon wafers. The cells feature a front-side boron diffusion (R_{sheet} ≈ 120 Ω/□) on random pyramid texturing, passivated by a SiN_x/Al_2O_3 stack. The planarized rear-sides of the cells were passivated with plasma-enhanced chemical vapor deposited SiN_x. The front contact openings were defined by photolithography and formed by a thermally evaporated Cr/Pd/Ag stack that was later thickened with additional Ag by electroplating. The rear-side contacts were also defined by photolithography prior to the TiO_2 ALD and Ca and Al metal evaporation procedures. The current–voltage (*J–V*) characteristics of the cells were measured using a Sinton Instruments FCT-450 flash tester which was calibrated using a certified reference cell from Franhaufer ISE CalLab.

Supporting Information

Supporting Information is available from the Wiley Online Library or from the author.

Acknowledgements

This work was supported by the Australian government through the Australian Renewable Energy Agency (ARENA). Work at the University of California, Berkeley was supported by the Bay Area Photovoltaic Consortium (BAPVC). The authors would like to acknowledge Sorin Lazar for his help with monochromated EELS experiments and the Interdisciplinary Centre For Electron Microscopy of EPFL for the use of their microscope.

Received: November 24, 2016
Revised: December 19, 2016
Published online:

[1] C. Battaglia, A. Cuevas, S. De Wolf, *Energy Environ. Sci.* **2016**, *9*, 1552.
[2] Z. C. Holman, A. Descoeudres, L. Barraud, F. Z. Fernandez, J. P. Seif, S. De Wolf, C. Ballif, *IEEE J. Photovolt.* **2012**, *2*, 7.
[3] NEDO: World's Highest Conversion Efficiency of 26.33% Achieved in a Crystalline Silicon Solar Cell, available at http://www.nedo.go.jp/english/news/AA5en_100109.html, accessed: September 2016.
[4] M. A. Green, *Sol. Energy Mater. Sol. Cells* **2015**, *143*, 190.
[5] J. Bullock, P. Zheng, Q. Jeangros, M. Tosun, M. Hettick, C. M. Sutter-Fella, Y. Wan, T. Allen, D. Yan, D. Macdonald, S. De Wolf, A. Hessler-Wyser, A. Cuevas, A. Javey, *Adv. Energy Mater.* **2016**, *6*, 1600241.
[6] T. G. Allen, J. Bullock, P. Zheng, B. Vaughan, M. Barr, Y. Wan, C. Samundsett, D. Walter, A. Javey, A. Cuevas, *Prog. Photovolt. Res. Appl.* **2016**.
[7] A. W. Blakers, A. Wang, A. M. Milne, J. Zhao, M. A. Green, *Appl. Phys. Lett.* **1989**, *55*, 1363.
[8] M. A. Green, A. W. Blakers, J. Zhao, A. M. Milne, A. Wang, X. Dai, *IEEE Trans. Electron Devices* **1990**, *37*, 331.
[9] J. Bullock, M. Hettick, J. Geissbuhler, A. J. Ong, T. Allen, C. M. Sutter-Fella, T. Chen, H. Ota, E. W. Schaler, S. De Wolf, C. Ballif, A. Cuevas, A. Javey, *Nat. Energy* **2016**, *1*, 15031.
[10] X. Yang, P. Zheng, Q. Bi, K. Weber, *Sol. Energy Mater. Sol. Cells* **2016**, *150*, 32.
[11] X. Yang, Q. Bi, H. Ali, K. Davis, W. V. Schoenfeld, K. Weber, *Adv. Mater.* **2016**, *28*, 5891.
[12] A. F. Thomson, K. R. McIntosh, *Prog. Photovolt. Res. Appl.* **2012**, *20*, 343.
[13] B. Liao, B. Hoex, A. G. Aberle, D. Chi, C. S. Bhatia, *Appl. Phys. Lett.* **2014**, *104*, 253903.
[14] J. Cui, T. Allen, Y. Wan, J. McKeon, C. Samundsett, D. Yan, X. Zhang, Y. Cui, Y. Chen, P. Verlinden, A. Cuevas, *Sol. Energy Mater. Sol. Cells* **2016**, *158*, 115.
[15] A. Richter, S. W. Glunz, F. Werner, J. Schmidt, A. Cuevas, *Phys. Rev. B* **2012**, *86*, 165202.
[16] S. Avasthi, W. E. McClain, G. Man, A. Kahn, J. Schwartz, J. C. Sturm, *Appl. Phys. Lett.* **2013**, *102*, 203901.
[17] K. A. Nagamatsu, S. Avasthi, G. Sahasrabudhe, G. Man, J. Jhaveri, A. H. Berg, J. Schwatz, A. Kahn, S. Wagner, J. C. Sturm, *Appl. Phys. Lett.* **2015**, *106*, 123906.
[18] D. K. Schroder, D. L. Meier, *IEEE Trans. Electron Devices* **1984**, *31*, 637.
[19] R. T. Tung, *Appl. Phys. Rev.* **2014**, *1*, 11304.
[20] R. Sinton, A. Cuevas, presented at *The 16th European Photovoltaics Solar Energy Conference*, Glasgow, Scotland **2000**.
[21] S. W. Glunz, J. Nekarda, H. Mackel, A. Cuevas, presented at *The 22nd European Photovoltaics Solar Energy Conference and Exhibition*, Milan, Italy **2007**.
[22] A. F. Carley, P. R. Chalker, J. C. Riviere, M. W. Roberts, *J. Chem. Soc. Faraday Trans. 1: Phys. Chem. Condens. Phases* **1987**, *83*, 351.
[23] S. Bartkowski, M. Neumann, E. Z. Fedorenko, S. N. Shamin, V. M. Cherkashenko, S. N. Nemnonov, A. Winiarski, D. C. Rubie, *Phys. Rev. B* **1997**, *56*, 10656.
[24] U. Diebold, *Surf. Sci. Spectra* **1996**, *4*, 227.
[25] Y. Gao, Y. Masuda, Z. Peng, T. Yonezawa, K. Koumoto, *J. Mater. Chem.* **2003**, *13*, 608.
[26] K. Siuzdak, M. Szkoda, M. Sawczak, A. Lisowska-Oleksiak, *New J. Chem.* **2015**, *39*, 2741.
[27] Q. Zhang, Y. Li, E. A. Ackerman, M. Gajdardziska-Josifovska, H. Li, *Appl. Catal., A* **2011**, *400*, 195.
[28] S. Tojo, T. Tachikawa, M. Fujitsuka, T. Majima, *J. Phys. Chem. C* **2008**, *112*, 14948.
[29] G. Bertoni, E. Beyers, J. Verbeeck, M. Mertens, P. Cool, E. F. Vansant, G. Van Tendeloo, *Ultramicroscopy* **2006**, *106*, 630.
[30] E. Stoyanov, F. Langenhorst, G. Steinle-Neumann, *Am. Mineral.* **2007**, *92*, 577.
[31] Q. Fu, T. Wagner, *J. Phys. Chem. B* **2005**, *109*, 11697.
[32] B. Demri, M. Hage-Ali, M. Moritz, J. L. Kahn, D. Muster, *Appl. Surf. Sci.* **1997**, *108*, 245.
[33] M. T. Greiner, M. G. Helander, W.-M. Tang, Z.-B. Wang, J. Qiu, Z.-H. Lu, *Nat. Mater.* **2011**, *11*, 76.
[34] A. Agrawal, J. Lin, M. Barth, R. White, B. Zheng, S. Chopra, S. Gupta, K. Wang, J. Gelatos, S. E. Mohney, S. Datta, *Appl. Phys. Lett.* **2014**, *104*, 112101.
[35] R. H. Cox, H. Strack, *Solid-State Electron.* **1967**, *10*, 1213.
[36] D. L. Meier, D. K. Schroder, *IEEE Trans. Electron Devices* **1984**, *31*, 647.